Propeller Source Noise Separation from Flight Test Measurements of the Joby Aviation Aircraft

Kyle A. Pascioni*
NASA Langley Research Center, Hampton, VA 23681

Austin D. Thai†, Jeremy J. Bain‡
Joby Aviation, Santa Cruz, CA 95060

The Vold-Kalman order-tracking filter is applied to full-scale acoustic flight test measurements of the Joby Aviation eVTOL aircraft. Using synchronized acquisition of the aircraft position, time-varying rotation rates of each propeller, and any given single-channel acoustic signal, harmonic and nonharmonic acoustic content can be separated. Furthermore, this time-domain technique can also separate harmonic content amongst individual propellers, providing additional physical insight into the total acoustic field. A 60 kt level flyover and hover are used to exemplify the effectiveness of the method. Results clearly demonstrate the ability to rank propulsors in terms of their relative importance without the use of phased arrays. Frequency- and order-domain results are provided, as well as noise hemispheres, to illustrate directivity and individual propeller contributions. Differences can be associated with interactional or installation effects due to the similarities in propeller states for each condition. Simulated signals that track the measured time-varying shaft rates were used to assess the proper filter pole count and bandwidth.

Nomenclature

a_0	Sound speed [ft/s]
A	Coefficient matrix of the structural equation
$A_{s,k}$	Amplitude of shaft s and order k for the simulated signal
f	Frequency vector, [Hz]
H	Multiorder difference matrix
I	Identity matrix
J_k	Loss function of the kth orders for VKF error minimization
k	Order index
K	Set of selected orders
$M_{t,s}$	Tip Mach number for shaft s
$M_{ref,s}$	Reference tip Mach number for shaft s
N_s	Number of shafts (propellers)
p	de-Dopplerized measured acoustic pressure [Pa]
$\hat{p}$	Harmonic acoustic pressure [Pa]
p_{ref}	Reference acoustic pressure [20 μPa]
p_{sim}	Simulated signal
r	VKF weighting coefficient
r_d	Propagation distance [ft]
s	Shaft (propeller) index
SPL	Sound pressure level [dB/Hz re. p_{ref}]
t	Reception time vector [s]

*Research Aerospace Engineer, Aeroacoustics Branch
†Acoustics Senior Engineer, Flight Physics
‡Aeroacoustics and CFD Lead, Flight Physics

x, y, z	Microphone array coordinates [ft]
$x_{s,k}$	Complex ampltiude envelope of shaft s and order k
Δf	Frequency binwidth [Hz]
$\varepsilon_{s,k}$	Error in VKF structural equation for shaft s and order k [Pa]
η	Nonharmonic (random) component of signal [Pa]
σ	Standard deviation
τ	Source-time vector [s]
$\Theta_{s,k}$	Complex phasor of shaft s and order k
ω_s	Rotation rate of shaft s [rev/s]

I. Introduction

Advanced Air Mobility (AAM) is a new and imminent sector in aviation primed to thrive in the coming years. In addition to safety, efficiency, and affordability, this emerging market needs to also have a good understanding of the other major barriers to integrate into existing communities.[1] Noise is one of the leading concerns and has ignited a growing number of research endeavors to investigate the physical acoustic generation mechanisms of these unique aircraft. While these studies are useful, they are often dedicated component tests of scaled geometry. Full-scale measurements are ultimately essential; however, with high degrees of freedom (e.g., propulsor tilt, blade pitch, rotation rate), novel measurement or processing techniques are needed to extract statistically significant trends from flight test data. This is particularly the case for vehicles with distributed electric propulsion in which each propulsor is independently controlled. In addition to vehicle state variability, a high acoustic sensitivity to atmospheric turbulence is also expected.[2]

Recently, NASA and Joby Aviation conducted a full-scale acoustic flight test[3] to characterize typical noise levels produced by the Joby Aviation preproduction prototype aircraft. These data provided a "first look" to the public and have since been leveraged to enhance acoustic prediction and modeling capabilities.[4] In an effort to further validate prediction methods and determine which sources dominate, the order tracking Vold-Kalman filter (VKF) will be applied in this paper. First introduced by Vold and Leuridan,[5] this time-domain technique has the ability to separate harmonic noise from nonharmonic noise of a single-channel acoustic measurement by tracking a complex phasor based on (known) individual time-varying rotation rates of each propulsor. Note that the term "harmonic noise" and "nonharmonic noise" will be used herein to refer to shaft-coherent and shaft-incoherent content, respectively. Additionally, the filter can be used to separate harmonic content amongst propulsors and overcomes temporal and frequency resolution tradeoffs of common spectral methods. With the aircraft in motion, short time segments of the acoustic pressure are typically defined to represent discrete emission angles. However, high frequency resolution is needed to identify or separate individual propulsor content. The combination of short time blocks with high frequency resolution can significantly increase uncertainty in the spectral representations. As will be shown, the VKF avoids these tradeoffs by tracking content in the order domain. Among others, Borghesani et al.[6] agrees with this sentiment, stating,

> "... it is clear that the monitoring of rotating machineries is by far more effective if analyses are performed in the angular domain of the shaft rotation, rather than in time domain. The same conclusion is valid for the order domain, the spectral counterpart of the angular domain (measured in n per revolution, nX), which is always preferred to the "Hertzian" frequency domain."

A number of examples of the VKF applied to aeroacoustics have proven its usefulness. For example, Truong[7] extracted tonal components from a small-scale ducted fan experiment to develop a novel exhuast fan source model. Shah et al.[8] extracted shaft-coherent content to independently study harmonic and nonharmonic content from a modern turbofan engine. More relevant to AAM, Tinney et al.[9] employed the VKF in conjunction with proper orthogonal decomposition to form a reduced order model of stacked rotors in hover. Truong et al.[10] found it useful to enable comparison with midfidelity predictions for an isolated rotor ground test. The method has also been shown to be robust to separate single-microphone measurements on a per-shaft basis. For example, Stephens and Vold[11] separated harmonic content of individual (not mechanically coupled) rotors from a counterrotating open rotor system and found the VKF more effective than phase averaging. From a psychoacoustic perspective, the ability to gain signal tonality relative to

broadband levels could support human response research into which sound quality metrics are predictive of annoyance.[12,13]

To the author's knowledge, the only acoustic flight test efforts to employ the VKF were performed by Rachaprolu and Greenwood,[14] and Rachaprolu et al.[15] For the former, effective separation of the main and tail rotor harmonic content of a Bell 430 helicopter was demonstrated. Individual time histories per rotor and full noise hemispheres characterized individual source directivity. The second effort was applied to a hexacopter in forward flight, which is the same number of propulsors in this work. Another similarity is the relatively close, and at times crossing, order frequencies amongst propulsors.

The remainder of this paper is organized as follows. First, the vehicle, flight conditions, and instrumentation are briefly covered. The Vold-Kalman method is then introduced and formulated as it is applied here. Synthetic signals with similar characteristics to the measurements are used to build confidence in the results and appropriately select filter parameters. Finally, results for both the flyover and hover conditions are provided. The readers are referred to the companion paper by Thai et al.[16] which compare these results to computational fluid dynamic simulations.

II. Vehicle

Joby Aviation has been developing an all-electric vertical takeoff and landing aircraft that is intended to operate as part of a fast, quiet, and convenient air taxi service. Joby first flew subscale flights in 2015 and its first full-scale prototype in 2017.[17] The preproduction prototype, which is the subject of this work and shown in Figure 1(a), has been undergoing flight tests since 2019. It is designed for high-density operations near residences and workplaces, where acoustics is of high importance. Additional nonproprietary details of the aircraft are provided in previous work.[4,17,18] Figure 1(b) provides the propeller numbering convention used throughout this paper.

(a) (b)

Figure 1. The Joby Aviation preproduction prototype aircraft (a) in transition and (b) the propeller numbering scheme as viewed from above. Photo credit: NASA

III. Instrumentation and Flight Conditions

For all acoustic measurements, 1/2" GRAS 67AX microphones embedded into 15" ground boards were used. Signal acquisition was accomplished by the second generation Wireless Acoustic Measurement System (WAMS2) with a sampling rate of 25 kS/s. Each flight condition will use a subset of microphones and will be discussed below. Additional details on instrumentation can be found in Pascioni et al.[3]

The aircraft performed a constant true airspeed level flyover at 60 kt, holding a condition somewhat representative of semithrust-borne flight during transition to forward flight. The six propellers were at a tilt of approximately 47° (VTOL mode defined to be 90°), similar to what is shown in Fig. 1(a). Fig. 2 provides the flight track geometry relative to a flyover subset of microphones that form a linear array perpendicular to the flight path. Figure 2(b) provides the azimuth and elevation angles covered as the aircraft maintained

370 ft altitude for a travel distance of +/- 2,000 ft. The majority of microphones map out port-side emission angles. Physical field constraints hindered additional measurements on the starboard side.

An out-of-ground effect hover was also conducted at an altitude of approximately 218 ft over the hover subset of the array. A time interval of 18 s during stable hover was chosen, during which the aircraft maintained its position nearly within one foot in all three directions. Figure 3 summarizes the vehicle position and heading relative to the microphones that will be used in later sections. Propellers were maintained at constant blade pitch and tilt in VTOL mode.

On-board vehicle data is crucial to the success of the methods described below. Position, attitude, and individual propeller states were recorded at 100 Hz and Coordinated Universal Time (UTC)-stamped to synchronize with the acoustic signals. Figure 4 provides the time varying rotation rates over the flyover and hover events.

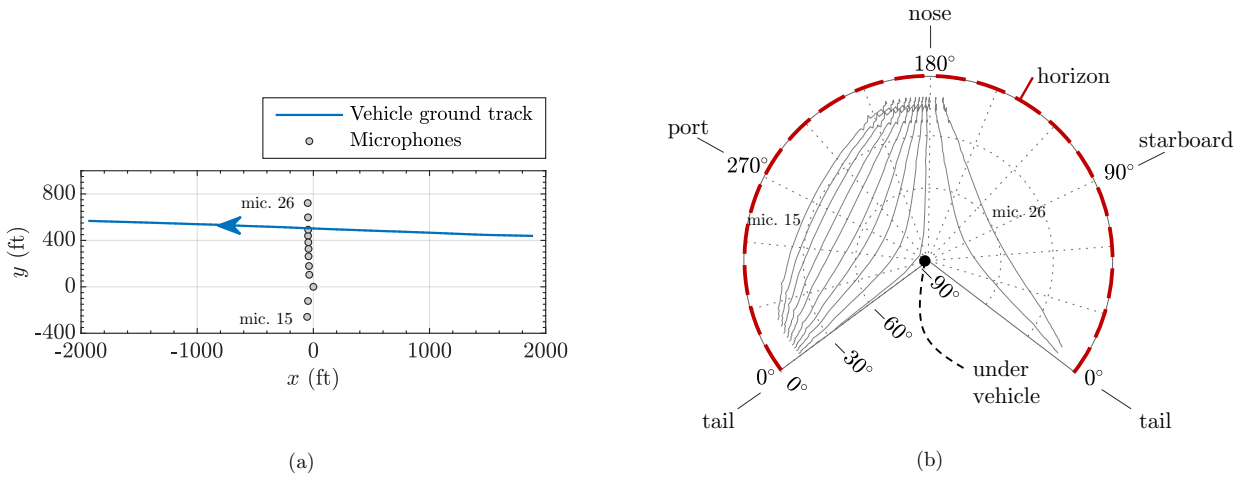

Figure 2. Geometry of the 60 kt flyover showing the (a) vehicle ground track relative to the flyover microphone subset with the direction of flight from right to left, and (b) the microphone traces over azimuth and elevation.

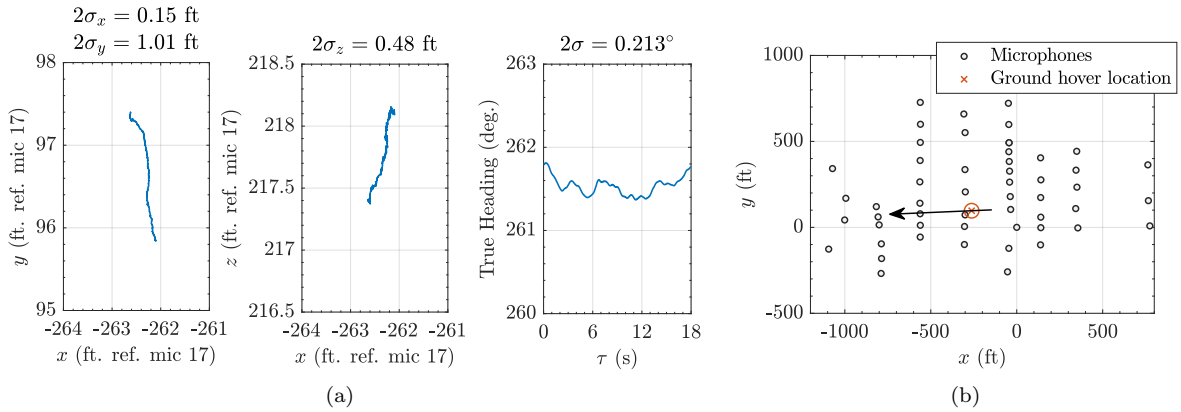

Figure 3. Aircraft (a) position and heading and (b) hover position over the microphone array. The arrow defines the heading pointing in the nose direction.

IV. Methods

IV.A. Preprocessing

The VKF tracks acoustic information that aligns with the shaft-order frequencies. The received signals, however, are Doppler shifted due to the moving source relative to the observer. For example, consider a source moving relative to a stationary observer emitting an impulse train. If the impulses are occurring at

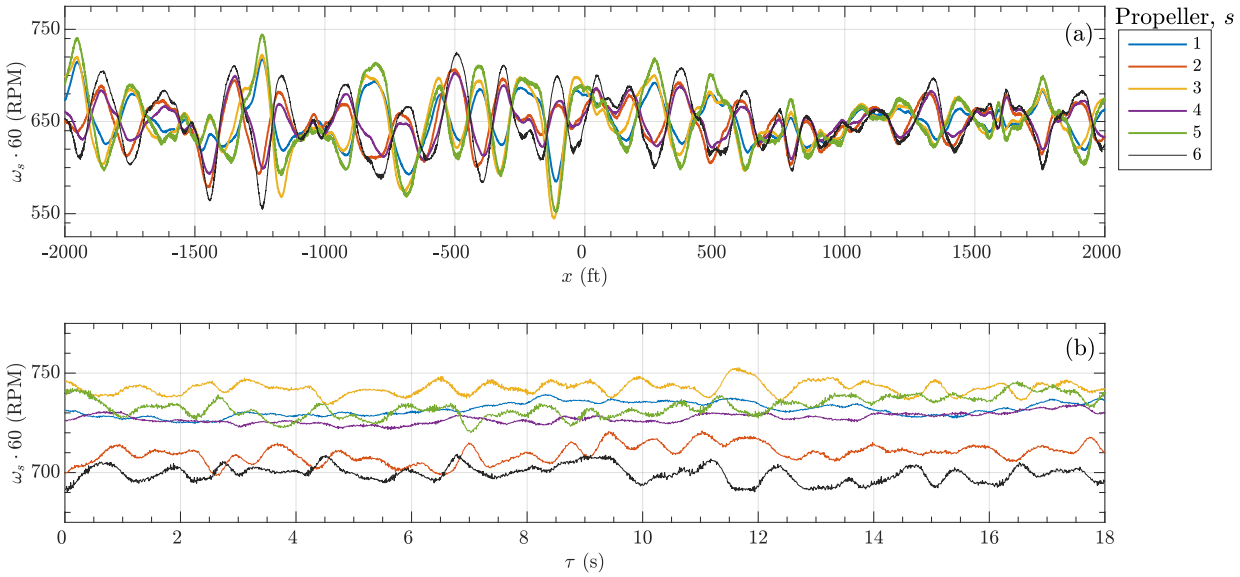

Figure 4. Individual propeller rotation rates for the (a) flyover and (b) hover cases. Note the difference in the ordinate scales.

a constant time interval, the impulses are received by the stationary observer at smaller intervals while the source is approaching, and at larger intervals when the source is receding. To remove this effect and align the measured signal frequencies with the propeller rotation rates, a time-domain de-Dopplerization technique[19] is applied to each microphone signal using the vehicle tracking data. The retarded time equation provides the relationship between reception and emission time, t and τ, respectively, for arbitrary relative movement,

$$\tau = t - r_d(\tau)/a_0, \tag{1}$$

in which $r_d(\tau)$ is the propagation distance from the vehicle center determined by the flight path at a given emission time and a_0 is the sound speed. A de-Dopplerized pressure time series is accomplished by interpolating the measured pressure time series at times τ. This transformation from reception to emission time results in a varying sampling rate of the resultant signal. For convenience, the emission time-based signal is interpolated to a constant sampling frequency of 20 kHz (20% reduction from the measured sampling rate). Note that convective amplification is not accounted for since it is a small effect ($\approx$ 1 dB or less) for the forward flight case.

The pressure time series amplitudes are also halved to account for the approximate sound-hard doubling of the ground board[20] and adjusted for spherical spreading to a reference distance of 100 ft from the aircraft center.

IV.B. Vold-Kalman Filter Overview

The second-generation multiorder version of the filter is chosen for this work. The mathematical formulation follows the work of several others.[7,9,21,22] Using the Wold decomposition, it can be assumed the measured de-Dopplerized acoustic pressure time series can be decomposed,

$$p(\tau) = \hat{p}(\tau) + \eta(\tau), \tag{2}$$

in which $\hat{p}(\tau)$ is shaft-coherent content and $\eta(\tau)$ is random and uncorrelated with any shaft (i.e., propeller) in the system. The total shaft-coherent information over a prescribed set of K orders (i.e., time-varying harmonics) is the superposition of those signals over N_s shafts,

$$\hat{p}(\tau) = \sum_{s=1}^{N_s} \sum_{k \in K} x_{s,k}(\tau) \Theta_{s,k}, \tag{3}$$

and

$$\Theta_{s,k}(\tau) = \exp\left(2\pi i k \int_0^{\tau} \omega_s(u)\mathrm{d}u\right). \tag{4}$$

The time-varying amplitude envelope, $x_{s,k}(\tau)$, is what the Vold-Kalman filter attempts to determine. The complex phasor in Equation 4 of order k tracks the time-varying rotational rate, $\omega_s(\tau)$, of shaft s, and is the result of an angular frequency integration. Note that these rates are required inputs that are known and sampled at a rate high enough to capture their variations. Plugging in Equation 3 into 2, and rearranging to form an error for the so-called data equation,

$$\eta(\tau) = p(\tau) - \sum_{s=1}^{N_s} \sum_{k \in K} x_{s,k}(\tau)\Theta_{s,k}(\tau). \tag{5}$$

Computer memory constraints inhibit simultaneously computing all orders over all shafts for the large number of samples in the measured signals. Therefore, a subset of orders is chosen and multiple instances of the filter are run consecutively. It is most important to compute orders together that have similar frequencies, particularly if those frequencies are close or momentarily cross. The benefit of coupling multiple shafts with similar order content is the suppression of beating phenomena.[23] To that end, the order subsets are chosen to be each order k for all propellers, yielding six waveforms ($N_s = 6$) to be simultaneously solved. Expanding Equation 5 for order k for all propellers (and dropping the k subscript) gives the following equation in matrix form,

$$\begin{bmatrix} \eta(\tau_1) \\ \eta(\tau_2) \\ \vdots \\ \eta(\tau_N) \end{bmatrix} = \begin{bmatrix} p(\tau_1) \\ p(\tau_2) \\ \vdots \\ p(\tau_N) \end{bmatrix} - \sum_{s=1}^{N_s} \begin{bmatrix} \Theta_s(\tau_1) & & & \\ & \Theta_s(\tau_2) & & \\ & & \ddots & \\ & & & \Theta_s(\tau_N) \end{bmatrix} \begin{bmatrix} x_s(\tau_1) \\ x_s(\tau_2) \\ \vdots \\ x_s(\tau_N) \end{bmatrix}. \tag{6}$$

A structural equation is also used to constrain envelope smoothness. To keep bandwidth small (small Δf), which will be discussed in the next section, the single-pole structural equation for time τ_i is formed using a difference equation,

$$\nabla^1 x_s(\tau_i) = x_s(\tau_i) - x_s(\tau_{i+1}) = \varepsilon_s(\tau_i), \tag{7}$$

which can also be cast in matrix form such that the finite difference coefficients form an upper bidiagonal matrix,

$$\begin{bmatrix} \varepsilon_s(\tau_1) \\ \varepsilon_s(\tau_2) \\ \vdots \\ \varepsilon_s(\tau_N) \end{bmatrix} = \begin{bmatrix} 1 & -1 & & & \\ & 1 & -1 & & \\ & & \ddots & \ddots & \\ & & & 1 & -1 \end{bmatrix} \begin{bmatrix} x_s(\tau_1) \\ x_s(\tau_2) \\ \vdots \\ x_s(\tau_N) \end{bmatrix}. \tag{8}$$

A loss function can now be defined using both errors from the data and structural equations, η and ε, respectively. For the kth order over all shafts, the loss function takes the form:

$$\begin{aligned} J &= r^2 \sum_{s=1}^{N_s} \varepsilon_s^T \varepsilon_s + \eta^T \eta \\ &= r^2 \sum_{s=1}^{N_s} x_s^H A^T A x_s + \left(p^T - \sum_{s=1}^{N_s} x_s^H \Theta_s^H\right)\left(p - \sum_{s=1}^{N_s} \Theta_s x_s\right), \end{aligned} \tag{9}$$

in which A is the coefficient matrix of Equation 8, and $(\cdot)^T$ and $(\cdot)^H$ denote the transpose and conjugate transpose, respectively. From Tuma,[21] the weighting factor for a second generation single-pole filter is defined by the desired bandwidth,

$$r \approx \sqrt{\frac{\sqrt{2}-1}{2(1-\cos(\pi\Delta f))}} \approx \frac{0.2048624}{\Delta f}. \tag{10}$$

The derivative of the loss function is taken with respect to the conjugate form of each amplitude envelope and set to zero to minimize the error,

$$\frac{\partial J}{\partial x_s^H} = 0 \text{ for } s = 1, 2, ..., N_s \tag{11}$$

to arrive at an equation for determining the kth order complex envelopes,

$$x(\tau) = \mathcal{H}^{-1}\Theta^H p(\tau), \tag{12}$$

in which

$$\mathcal{H}_{sq} = \begin{cases} r^2 A^T A + I & \text{for } s = q \\ \Theta_s^H \Theta_q & \text{for } s \neq q. \end{cases} \tag{13}$$

Equation 12 is solved using the Cholesky solver of the Matlab backslash operator, and is called N_k times. Once the complex envelopes are known, Equation 3 can be used to determine the harmonic content, $\hat{p}$.

IV.C. Selection of Filter Characteristics

The optimal pole count and bandwidth (defining r in Equation 10) are case-dependent. A two-pole filter is most commonly found in the literature as it provides a good middle ground between roll-off behavior and numerical stability. However, there is a limitation on how small the bandwidth can be before the numerics become ill-conditioned, and an increasing limitation with pole count. In this work, a small bandwidth is desired given how close the propeller rotation rates (thus, order frequencies) are relative to each other. Therefore, a single-pole filter is selected.

A known simulated signal is generated to understand the effect of bandwidth. To be directly applicable to the measurements, a signal with similar characteristics is formulated,

$$p_{\text{sim}}(t) = \sum_{s=1}^{N_s} \sum_{k \in K} A_{s,k} \left(\frac{M_{t,s}(t)}{M_{ref,s}} \right)^4 \text{Re} \left\{ \exp \left(2\pi i k \int_0^t \omega_s(u) \text{d}u \right) \right\} + \eta(t). \tag{14}$$

The fundamental blade passage frequencies (BPFs) of the six propellers typically have the largest amplitudes in the measurements relative to their harmonics and subharmonics. To emulate this, the amplitudes are set to be $A_{s,k} = \{1/4, 1/2, 1(\text{BPFs}), 1/2, 1/4, 1/8, 1/16\}$ for all six simulated shafts, s, and $k = 2, 3, 5, 10, 15, 20, 25$. To introduce amplitude variation, the amplitude is scaled by the instantaneous tip Mach number of each individual shaft and tracks the measured unsteady rotation rates, ω_s, of the measurements for the hover case (Fig. 4(b)). The power of four was chosen to be in the range of previous power law scalings for tonal content of a propeller.[24] Additional random (nonharmonic) noise, $\eta(t)$, is added and follows the typical broadband shelf of the measurements, defined by its peak being 20 dB down from the BPF amplitudes, $A_{s,5}$. The spectral shape of the added noise is defined by applying a first order Butterworth bandpass filter to a random white noise signal using frequency cutoffs of 20 and 100 Hz.

Figure 5 demonstrates the effect of VKF bandwidth by comparing the spectral representations of the full simulated signal, p_{sim}, the known harmonic content, $p_{\text{sim}} - \eta$, and the filter-extracted harmonic content, $\hat{p}$. For the largest bandwidth, the filter overextracts energy at the lowest orders because it lacks resolution, i.e., the bandwidth is significantly larger than the difference in harmonic frequencies amongst shafts. The second largest bandwidth provides a better estimate of harmonic levels; although, the difference between the simulated signal and filter-extracted content, $p_{\text{sim}} - \hat{p}$, which should bypass random noise, shows clear divots at the order frequencies. These divots, which should be avoided as suggested by Truong et al.,[10] indicate the filter is inappropriately extracting random noise along with the harmonic components. The smallest bandwidth is most suitable and provides a good estimate of harmonic levels while showing indifference to the random noise. For the results in the following section, the bandwidth will be chosen with this thought process in mind.

Given that the simulated signal is a superposition of six independent waveforms, each composed of seven harmonic orders, the total signal is very complex with no apparent repeating waveform pattern over the nominal shaft period. Figure 6 compares the filter-extracted content with the full simulated signal, both with and without random noise, for the best performing bandwidth from Figure 5(c). The filter does an outstanding job of estimating the amplitude- and frequency-varying total waveform in the time domain. Individual shaft waveforms also compared favorably. These results provide confidence in applying this method to measurements in which the true levels of the harmonic content are unknown. Although this paper does not include time-domain results for the measurements, this filter could prove extremely valuable to extract waveforms, per shaft,[14] for direct comparison with prediction tools.

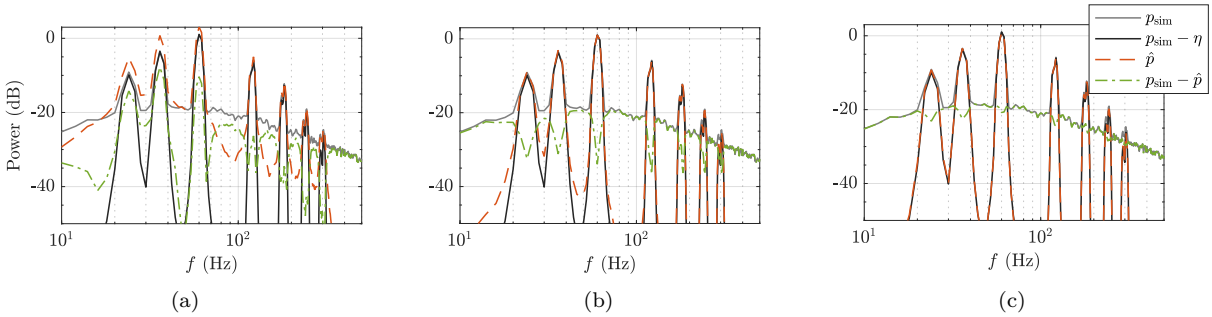

Figure 5. Effect of extracting harmonic components from a known simulated signal with decreasing filter bandwidth from (a) to (c).

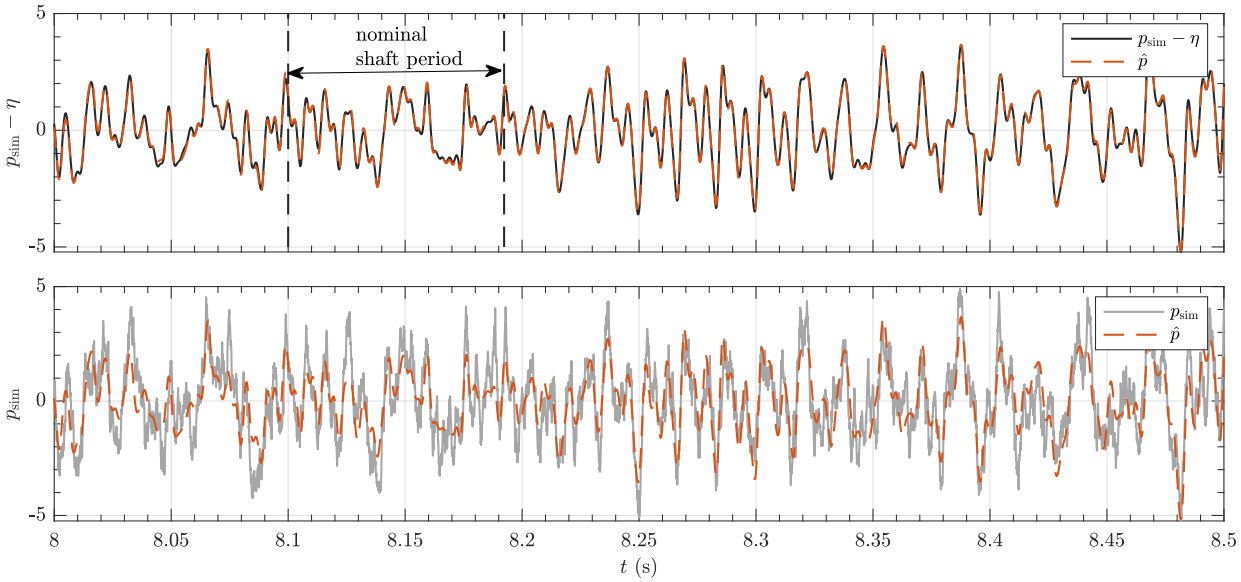

Figure 6. Time-domain comparison over an arbitrarily chosen segment between the filter-extracted content and the simulated signal (a) without and (b) with random noise. Note that both cases applied the filter to the simulated noisy signal.

V. Results

The Vold-Kalman filter will now be applied to the flight test measurements. Following the procedure of selecting the bandwidth to maintain the estimated broadband shelf for appropriate harmonic extraction, a bandwidth of 1 Hz was selected for all results to follow. All acoustic data are scaled to a reference distance of 100 ft. from the aircraft center and corrected for atmospheric absorption.[25] Integrated sound pressure levels (SPL) use frequency bins from 12 Hz to 2 kHz.

V.A. Semithrust-Borne Forward Flight

An overview of the data is given in spectral form for various emission angles in Figure 7 using 0.5 s blocks of data. Each plot compares the spectral estimates of the original de-Dopplerized signal, the harmonic content identified by the VKF summed over all shafts and orders, and the residual. This residual is the time-domain difference between the original and total VKF signal. The harmonic content has similar levels to the original signal at low shaft orders (frequencies). The difference between these increase with order,

which is expected since the higher-order levels approach nonharmonic levels. The fundamental blade passage frequencies ($k = 5$) are found to dominate the spectra over most emission angles, with the exception being far aft of the vehicle. The spectra here are representative of other microphones in the flyover subset, which produce similar trends. The bar charts represent the total energy of the harmonic content per shaft for each emission angle. The tail propellers are identified as the dominant contributors, particularly in front of and underneath the aircraft, as compared to the four wing propellers.

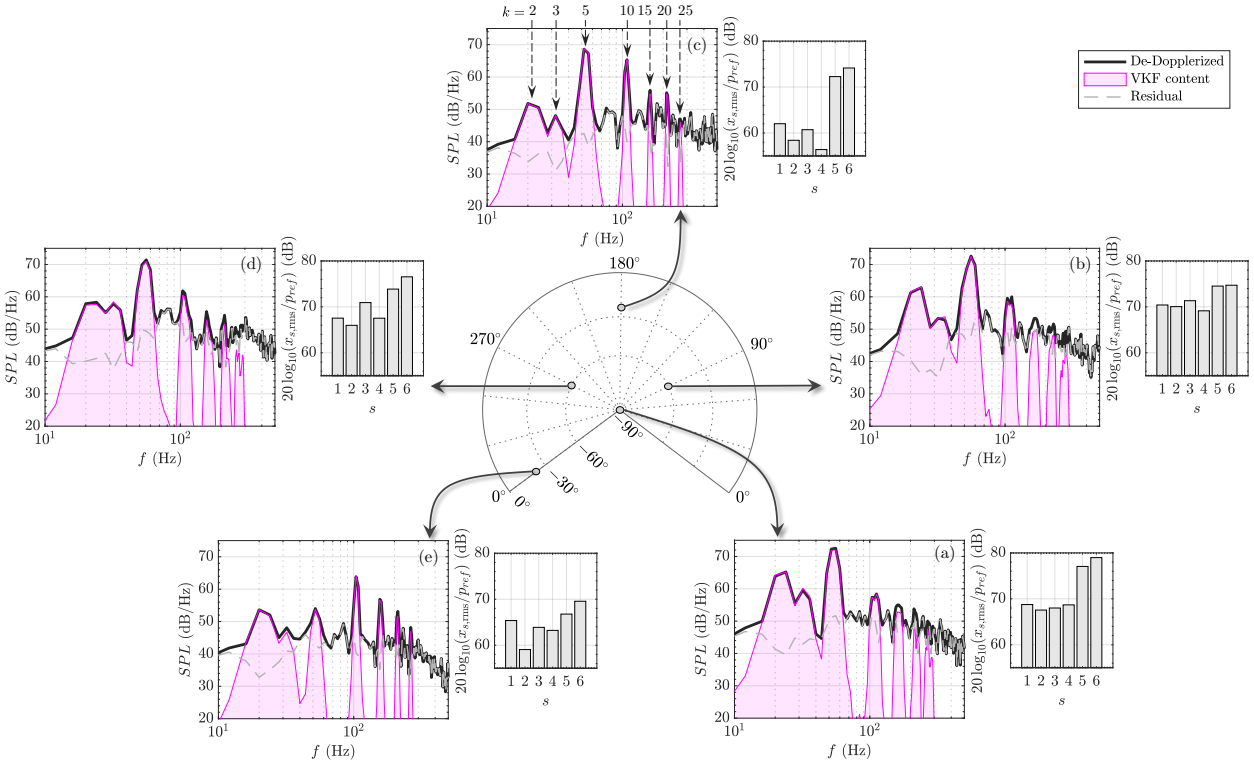

Figure 7. Vold-Kalman filter-extracted content separated into individual propeller contributions for a 60 kt level flyover (a) under the vehicle, (b) starboard, (c) in front of, (d) port, and (e) aft.

It is also worthwhile to view these data over all measured observer angles. Contours of integrated sound pressure levels are given in Figure 8. Again, the original de-Dopplerized signals (Fig. 8(a)) can be compared to the harmonic content (Fig. 8(b)). The directivity features look similar, which is expected given the dominance of the harmonic information. The largest levels are found underneath the vehicle with the lowest levels in front of the vehicle. The residual is again plotted in Fig. 8(c). At first glance, the directivity pattern looks similar to what would be expected from broadband self-noise, peaking at angles aft of the aircraft. Accounting for propeller tilt, these aft angles correspond to out-of-plane angles with respect to the propellers. Broadband noise likely dominates this residual, although there could be additional orders that were not extracted. Removing all harmonic content would enable the residual to be a useful broadband characterization and has been conducted by others.[7,14]

Perhaps the most interesting visualization is a plot of individual propeller harmonic content over all measured emission angles (Fig. 9). The four propellers along the wing are similar in their peak levels. They also exhibit similar directivity patterns with highest levels either along or just aft of the 90°-270° azimuths, which emanate out from the starboard and port wings, respectively.

As compared to the wing propellers, the tail propellers produce nearly 10 dB higher peak levels, with peak levels found more aft. What makes this even more noteworthy is that the rotation rates, tilt, and blade pitch were all, on average, very close over all propellers, indicating the resulting noise difference is an aerodynamic interaction or installation effect. As shown in the spectra of Fig. 7, the blade passage frequencies, which dominate the overall harmonic levels, have a wavelength on the order of a semispan. Thus, acoustic scattering may not be the driver in these differences. Speculating for a moment, the tail propellers may produce more noise due to interactional effects, particularly if they are ingesting nonuniform inflow due to the wake of

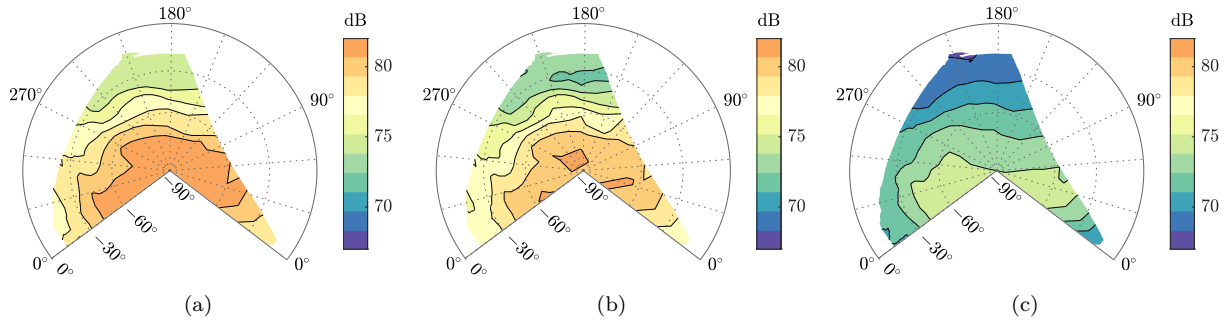

Figure 8. Hemisphere representation of overall sound pressure levels of the (a) de-Dopplerized signal, (b) the total Vold-Kalman filter-extracted content, and (c) the residual. Condition is a 60 kt level flyover.

the inboard propellers. The computational companion paper by Thai et al.[16] may help in understanding the physics at play, given the reasonably good comparison between the measurements and their simulations, which can be found in Fig. 10. In any case, this type of source ranking can be invaluable to researchers to design quieter vehicles, validate prediction tools, apply noise reduction technologies, etc.

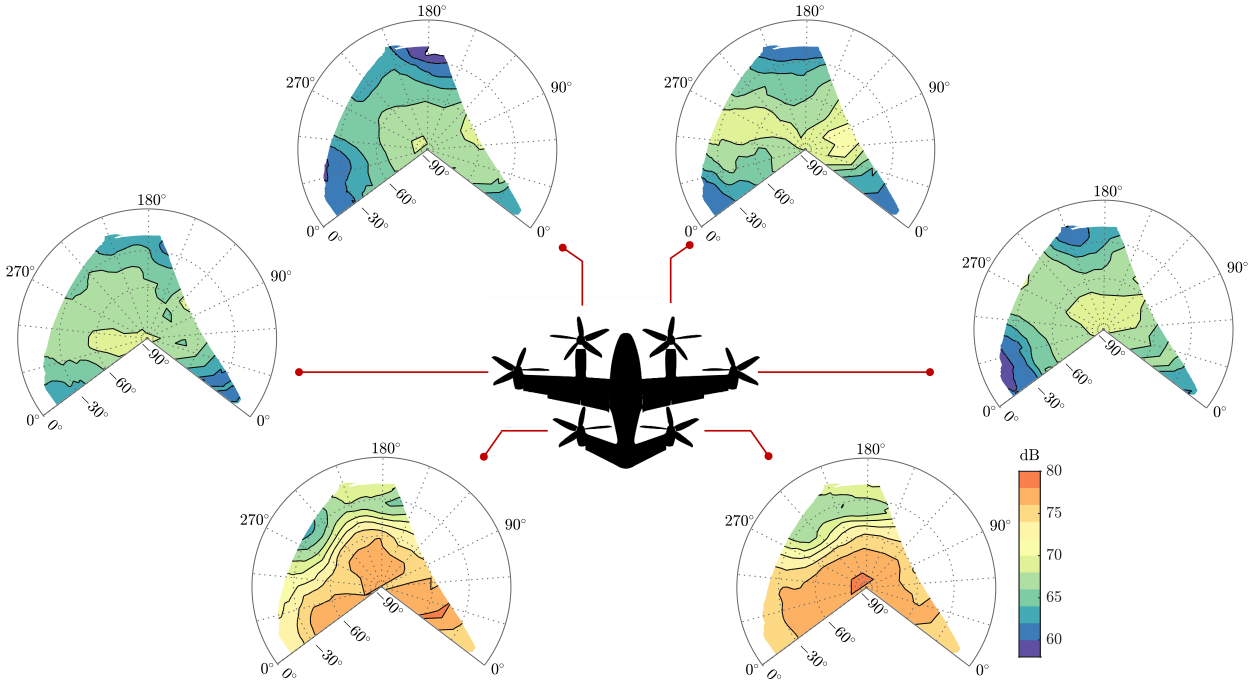

Figure 9. Vold-Kalman filter-extracted content separated into individual propeller contributions for a 60 kt level flyover.

V.B. Hover

Additional assessments of the VKF method took advantage of the hover condition to simplify the relative geometry between the microphones and aircraft. The rotation rates exhibited more steadiness relative to the forward flight case, as evidenced by Fig. 4, further simplifying the situation. To ensure the extraction/separation process was tracking the appropriate order frequency content, the peak spectral harmonic frequencies of the individual propellers were compared to the distributed rotation rates. Figure 11 plots spectral estimates of the individual propeller waveforms over a one second segment of data. The binwidth was decreased to enhance frequency resolution. Focusing on the highest order extracted (≈300 Hz) as it provides the largest frequency spread, the corresponding individual rotation rates are paired with the harmonic peaks. These peaks successfully correspond to the appropriate propeller.

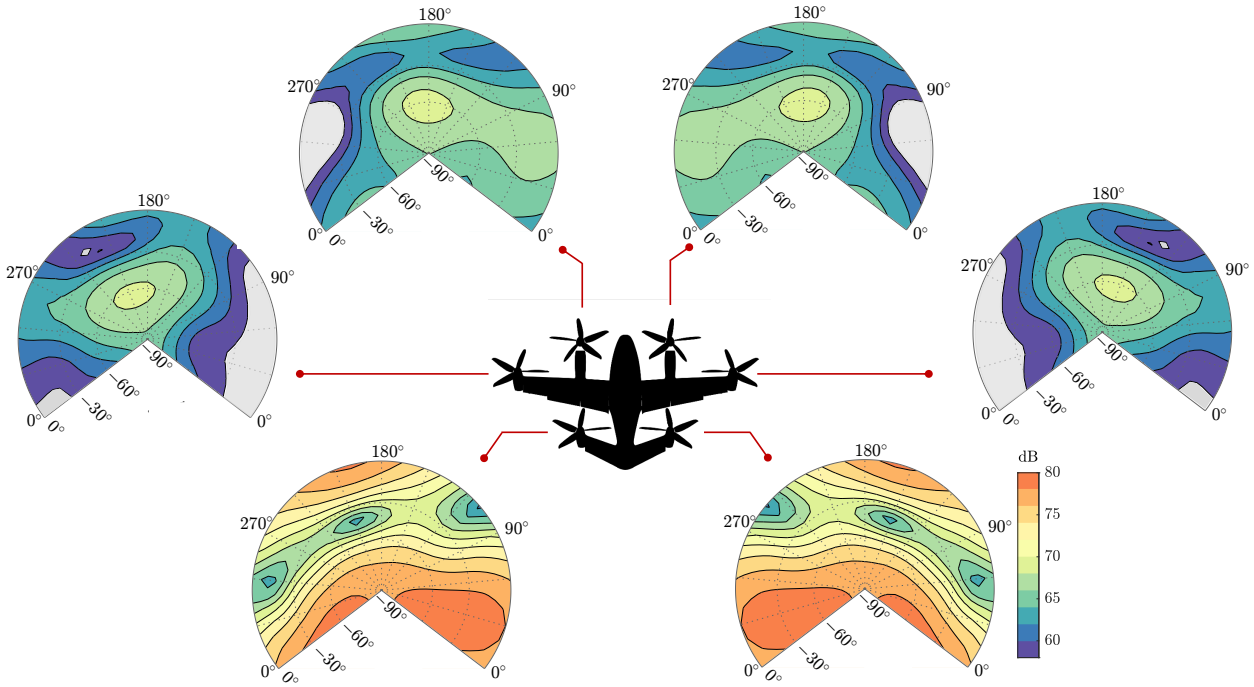

Figure 10. Individual propeller acoustic hemispheres from numerical simulations[16] integrated over the shaft orders extracted in Fig. 9.

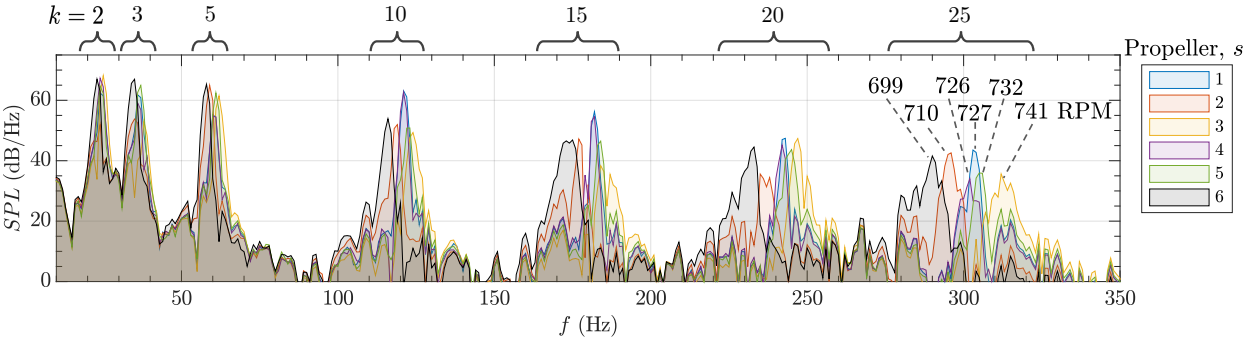

Figure 11. High resolution spectra of the harmonic content of each propeller obtained using the VKF. Mean rotation rates are given and correctly correspond to the appropriate propeller.

To visualize the extraction over the full duration of the hover, spectrograms are provided in Fig. 12 for a single microphone directly under the aircraft. The original signal has content over a broad frequency range, with peaks that correspond to the shaft orders. The residual clearly shows the removal of the majority of energy at the shaft orders. Note the absence of any signs that overextraction occurs at the shaft orders by the lack of the aforementioned spectral divots in the broadband content. Other microphones indicated similar behavior.

With the aircraft not in motion, the hemisphere representation found in the previous section is less useful. Instead, the majority of deployed microphones are used to produce contours over the ground plane to illustrate directivity features. All levels are again scaled to a reference observer of 100 ft to de-emphasize spherical spreading. Atmospheric absorption is also accounted for. Figure 13 plots individual propeller contributions over an area of approximately 2,000 by 1,000 ft. In these plots, the vehicle (not to scale) is shown to indicate its stabilized heading.

There are several interesting features that can be observed. Similar to the forward flight case, the tail propellers generate the highest levels of harmonic noise, although the difference with the wing propellers

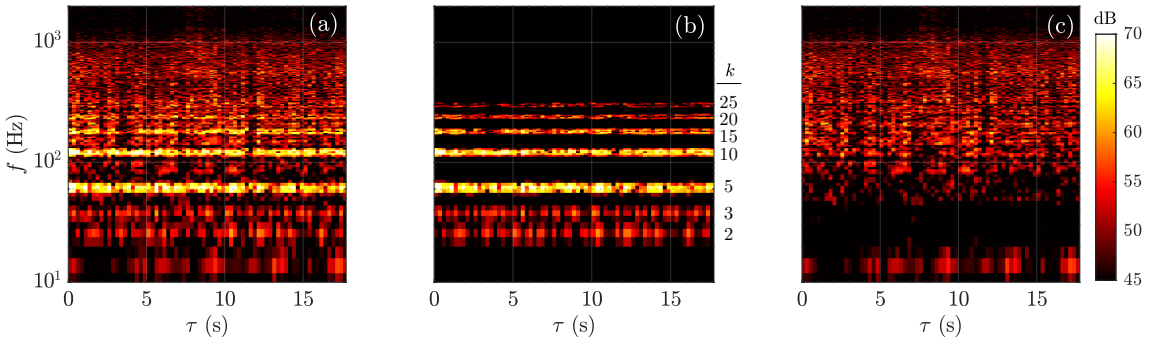

Figure 12. Spectrograms of the (a) original, (b) harmonic content, and (c) residual signals over the full duration of the hover event for a microphone directly underneath the vehicle.

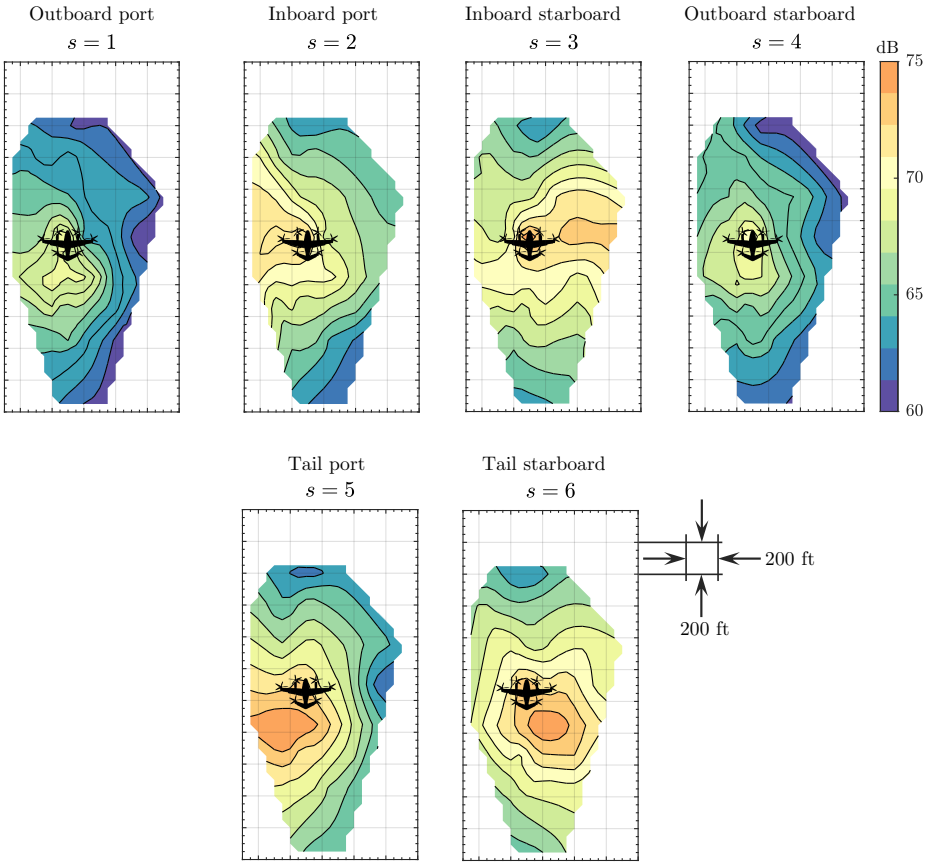

Figure 13. Ground contours of Vold-Kalman filter-extracted content separated into individual propeller contributions for hover. Outboard, inboard, and tail propeller pairs produce similar radiation patterns as mirrored about the longitudinal vehicle axis. Vehicle silhouette (not to scale) indicates its heading, and levels are all scaled to a 100 ft observer distance.

is not as large. The inboard propellers are identified as the secondmost dominant pair, with the outboard propellers producing the lowest levels. Focusing attention to directivity, the symmetric pairs of propellers are found to generate somewhat symmetric patterns. For example, the tail pair show peak radiation in their respective aft quadrants, and the inboard pair produce peak radiation toward their respective sideline directions. The outboard pair indicate peak levels below the aircraft with less bias in any given direction

relative to the other propellers. The fact that each pair have directivities that resemble one another builds confidence that the filter is appropriately separating content amongst the propellers.

Because the aircraft is static, aerodynamic interaction between propellers is not as likely. The lack of forward motion and the fact that the tilt angles correspond to a VTOL configuration indicates there is also no wake interference between wing and tail propellers. Rotation rates for all propellers are within approximately 50 RPM, and tilt and blade pitch are all also nearly identical. Thus, propeller/airframe interaction, and the differences in proximity to various airframe geometry, may be responsible for the aeroacoustic differences amongst propeller pairs. These observations highlight the fact that installed propellers can be very different than their isolated counterparts, both in terms of directivity patterns and peak levels.

Two repeats of this hover test point were also acquired. Individual propeller directivity and peak levels were similar to what is shown in Fig. 13. To summarize these data, Fig. 14 displays the dominant propeller over the ground area. This ranking is based on the root-mean-square of the individual propeller signals summed over the set of harmonics. For each of these test points, the tail propellers repeatedly dominated aft observers in a similar fashion. The observers in front of the aircraft had a mixture of the inboard and tail propellers with some spatial variation over the repeats. One interesting result is the lack of dominance from the outboard propellers, further concluding their relatively lower level signatures during hover.

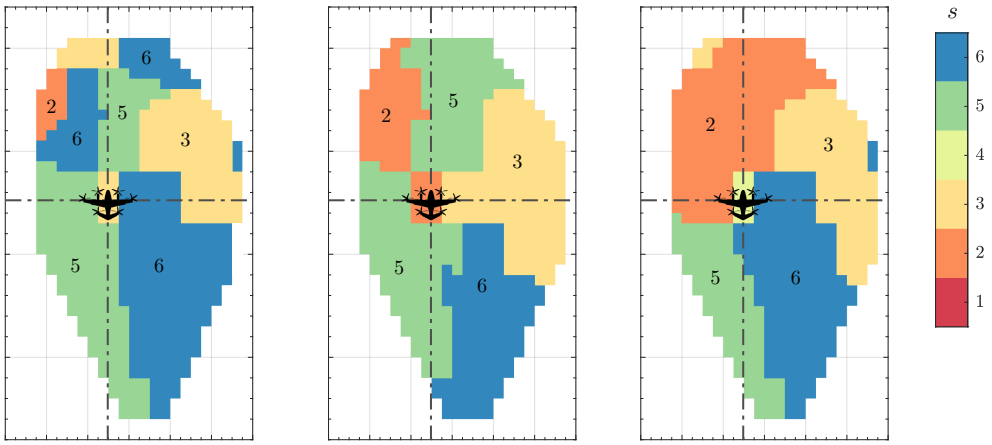

Figure 14. Area of ground contour displaying which propeller dominated over three independent hover runs. The run on the left is the main case used in this paper.

VI. Concluding Remarks

This paper applies the Vold-Kalman filter to full-scale eVTOL flight test measurements in an attempt to separate harmonic content among the individual propellers from single-channel acoustic signals. Being case dependent, the pole count and bandwidth were assessed using simulated signals with characteristics similar to the measurements. Spectra and source hemispheres were compared between the original signals and shaft-hamonic content. For the 60 kt flyover, the tail propellers produce noise levels nearly 10 dB higher than the wing propellers, and levels are consistent with numerical simulations. These increased levels are an indication of aerodynamic interaction or installation effects, particularly because propeller states were nearly identical across the set. Hover directivity patterns of the harmonic content were assessed using ground noise contours. The propellers on the port side show similar but mirrored patterns to their respective starboard complement. Given the lack of forward motion during hover, wake interaction between the front and aft propellers is unlikely. Thus, the differences in levels and patterns amongst the propellers are likely the result of aerodynamic or acoustic interaction with the airframe. Repeatability was demonstrated by comparing propeller dominance over the ground contour of three hover events. These type of source noise separation methods are likely to be an invaluable tool when understanding the dominant noise generating mechanisms, without the use of a phased array, and improving prediction tools to account for interaction or installation effects. While it is still uncertain if the harmonic noise highlighted in this paper is important from a psychoacoustic perspective, future response studies could leverage this signal decomposition method by scaling content relative to nonharmonic components.

Acknowledgments

The authors would like to thank Dr. Nikolas Zawodny for the discussions throughout the implementation of this effort. The authors also appreciate the motivating and influential conversations with Dr. Parthiv Shah. This work was supported by the NASA Aeronautics Research Mission Directorate, Revolutionary Vertical Lift Technology Project.

References

[1]"NASA Aeronautics Research Mission Directorate Strategic Implementation Plan," https://www.nasa.gov/directorates/armd/armd-strategic-implementation-plan/, Accessed: 2023-11-7.

[2]Fleming, J., Langford, M., Gold, J., Schwartz, K., Wisda, D., Alexander, N., and Whelchel, J., "Measured Acoustic Characteristics of Low Tip Speed eVTOL Rotors in Hover," *Vertical Flight Society 78th Annual Forum & Technology Display*, May 2022.

[3]Pascioni, K., Watts, M., Houston, M., Lind, A., Stephenson, J., and Bain, J., "Acoustic Flight Test of the Joby Aviation Advanced Air Mobility Prototype Vehicle," *28th AIAA/CEAS Aeroacoustics Conference*, AIAA Paper 2022-3036, 2022.

[4]Thai, A., Bain, J., Mikić, G., and Stoll, A., "Flyover Noise Computations of the Joby Aviation Aircraft," *Vertical Flight Society 79th Annual Forum & Technology Display*, May 2023.

[5]Vold, H. and Leuridan, J., "High Resolution Order Tracking at Extreme Slew Rates using Kalman Tracking Filters," *SAE Technical Paper 931288*, 1993.

[6]Borghesani, P., Pennacchi, P., Chatterton, S., and Ricci, R., "The Velocity Synchronous Discrete Fourier Transform for Order Tracking in the Field of Rotating Machinery," *Mechanical Systems and Signal Processing*, Vol. 44, No. 1-2, 2014, pp. 118–133.

[7]Truong, A., *Experimental and Theoretical Investigation of the Emission and Diffraction of Discrete Tone Noise Generated from the Exhaust of a Ducted Fan*, Ph.D. thesis, UC Irvine, 2018.

[8]Shah, P., Vold, H., Hensley, D., Envia, E., and Stephens, D., "A high-resolution continuous-scan acoustic measurement method for turbofan engine applications," *Journal of Turbomachinery*, Vol. 137, No. 12, 2015.

[9]Tinney, C., Zhao-Dubuc, Y., and Valdez, J., "The space-time structure of sound produced by stacked rotors in hover using Vold-Kalman filters and proper orthogonal decomposition," *International Journal of Aeroacoustics*, 2023.

[10]Truong, A., Johnson, C., and Sirohi, J., "Hovering Medium Sized UAM Rotor Noise Experiments and Multifidelity Predictions," *AIAA AVIATION 2023 Forum*, AIAA Paper 2023-4520, 2023.

[11]Stephens, D. and Vold, H., "Order tracking signal processing for open rotor acoustics," *Journal of Sound and Vibration*, Vol. 333, No. 16, 2014.

[12]Boucher, M., Rafaelof, M., Begault, D., Christian, A., Krishnamurthy, S., and Rizzi, S., "A Psychoacoustic Test for Urban Air Mobility Vehicle Sound Quality," *SAE Technical Paper 2023-01-1107*, 2023.

[13]Tracy, T., Boucher, M., Christian, A., Krishnamurthy, S., Rizzi, S., Begault, D., and Shepherd, K., "An Annoyance Model for Urban Air Mobility Vehicle Noise in the Presence of a Masker," *NOISE-CON Congress and Conference Proceedings*, 2024.

[14]Rachaprolu, J. and Greenwood, E., "Helicopter noise source separation using an order tracking filter," *Journal of the American Helicopter Society*, Vol. 69, No. 012006, 2023.

[15]Rachaprolu, J., Valente, V., El Sharkawy, E., and Greenwood, E., "Multirotor Noise Source Separation and Characterization from Ground-Based Acoustic Measurements," *Vertical Flight Society 80th Annual Forum & Technology Display*, May 2024.

[16]Thai, A., Bain, J., and Pascioni, K., "Identification and Computation of Individual Propeller Acoustics of the Joby Aviation Aircraft," *30th AIAA/CEAS Aeroacoustics Conference*, AIAA Paper, 2024.

[17]Stoll, A. and Bevirt, J., "Development of eVTOL Aircraft For Urban Air Mobility At Joby Aviation," *Vertical Flight Society 78th Annual Forum & Technology Display*, May 2022.

[18]Bain, J., Mikić, G., and Stoll, A., "Aerodynamic And Acoustic Design Of The Joby Aviation eVTOL Propeller," *Vertical Flight Society 77th Annual Forum & Technology Display*, May 2021.

[19]Greenwood, E. and Schmitz, F., "Separation of main and tail rotor noise from ground-based acoustic measurements," *Journal of Aircraft*, Vol. 51, No. 2, 2014, pp. 464–472.

[20]Nesbitt, E., Lan, J., and Hunkler, S., "Microphone Acoustic Characteristics for Aircraft Flyover Testing," *AIAA AVIATION 2020 Forum*, AIAA Paper 2020-2613, 2020.

[21]Tůma, J., "Setting the passband width in the Vold-Kalman order tracking filter," *12th International Congress on Sound and Vibration (ICSV12)*, 2005.

[22]Tůma, J., "Algorithms for the Vold-Kalman multiorder tracking filter," *Proceedings of the 14th International Carpathian Control Conference (ICCC)*, IEEE, 2013, pp. 388–394.

[23]Feldbauer, C. and Holdrich, R., "Realization of a Vold-Kalman tracking filter—a least squares problem," *Proceedings of the COST G-6 Conference on Digital Audio Effects*, 2000, pp. 1–4.

[24]Pascioni, K. and Rizzi, S., "Tonal Noise Prediction of a Distributed Propulsion Unmanned Aerial Vehicle," *24th AIAA/CEAS Aeroacoustics Conference*, AIAA Paper 2018-2951, 2018.

[25]Bass, H., Sutherland, L., Zuckerwar, A., Blackstock, D., and Hester, D., "Atmospheric absorption of sound: Further developments," *The Journal of the Acoustical Society of America*, Vol. 97, No. 1, 1995, pp. 680–683.